Journal of Applied Fluid Mechanics, Vol. 17, No. 8, pp. 1593-1603, 2024.
Available online at www.jafmonline.net, ISSN 1735-3572, EISSN 1735-3645.
https://doi.org/10.47176/jafm.17.8.2591

Research on the Flow and Drag Reduction Characteristics of Surfaces with Biomimetic Fitting Structure

C. Hu, Y. Gu†, J. Zhang, Q. Qiu, H. Ding, D. Wu, and J. Mou

College of Metrology Measurement and Instrument, China Jiliang University, Hangzhou, 310018, China
Zhejiang Engineering Research Center of Fluid Equipment and Measurement and Control Technology, Hangzhou, 310018, China

†Corresponding Author Email: guyunqing@cjlu.edu.cn

ABSTRACT

To reduce the fluid resistance on the surface of flow-through components and improve energy utilization efficiency, a biomimetic fitting structure model is constructed based on the ridge-like features of beluga skin. The SST k-ω model is employed to numerically simulate the drag reduction characteristics of three biomimetic structures (fitting structure, V-shaped structure, and arc structure) included in the design. The variations of the fitting structure's viscous resistance and pressure drop resistance with different widths and depths are compared. The drag reduction mechanism of the fitting structure surface is studied based on the pressure stress, velocity field, and shear stress. The results demonstrate that the fitting structure exhibits the best drag reduction performance. The fitting structure with a width of 30 mm and a depth of 0.7 mm achieves an optimal drag reduction effect of 4.18%. The fitting structure exhibits a large low shear stress region, which increases the thickness of the bottom boundary layer, thereby reducing surface velocity and viscous resistance.

Article History

Received January 15, 2024
Revised February 23, 2024
Accepted March 8, 2024
Available online May 29, 2024

Keywords:

Fitting structure
Drag reduction
Numerical simulation
Surface flow field

1. INTRODUCTION

The existence of turbulence greatly increases the resistance of ships, submarines and other marine equipment during travel, leading to substantial energy loss to overcoming the resulting surface drag. Research on surface drag reduction technology is of significant practical significance for improving the energy efficiency of marine equipment, increasing the navigation time (Wu et al., 2020), reducing surface wear (Gu et al., 2022a), and assisting in achieving the goal of a "carbon peak and carbon neutrality".

Currently, the main drag reduction techniques include surface coating drag reduction, nonsmooth surface drag reduction and jet stream drag reduction. Surface coating drag reduction covers a layer of continuous, dense coating film on an object's surface to change the surface hydrophobicity and vortex effect, such as that caused by the addition of polymers (Xie et al., 2023) and active agents (Yang et al., 2020). Nonsmooth surface drag reduction is a focus of turbulence drag reduction technology, which seeks to reduce wall friction by constructing wall surface structures with different features based on biomimetic principles to influence the organization of the boundary layer (Liu et al., 2020), such as microgrooves (Mele, 2022; Gu et al., 2023a) and adaptive walls (Chae et al., 2019; Deshpande et al., 2024). Jet stream drag reduction is a method for realizing the control of the wall boundary layer by injecting fluid media onto the surface of an object, such as gas jets (Desai et al., 2020) or underwater jets (Gu et al., 2023b). Various drag reduction techniques have varying principles of implementation, as well as differences in their applicability and drag reduction efficiency (Yu, 2021). Surface coating drag reduction is prone to environmental pollution, and jet stream drag reduction requires external energy injection, both of which tend to incur a large cost, while a nonsmooth surface overcomes this effect, and its applicability is wider (Ma et al., 2024). By analyzing the structure of shark body surfaces, researchers have proposed a nonsmooth rib-like groove structure (Meng et al., 2016). Since then, researchers have conducted many studies on groove structure (Deng et al., 2022). Inspired by shark skin, researchers (Liu et al., 2023) have investigated the drag reduction characteristics of V-shaped groove structures through particle image velocimetry (PIV) experiments and finite volume method (FVM) simulations, and the results showed that at lower free stream velocities, V-shaped grooves with an adjacent height ratio of 1:1 can achieve the optimal drag reduction effect. The addition of ridge-like structures on the surface

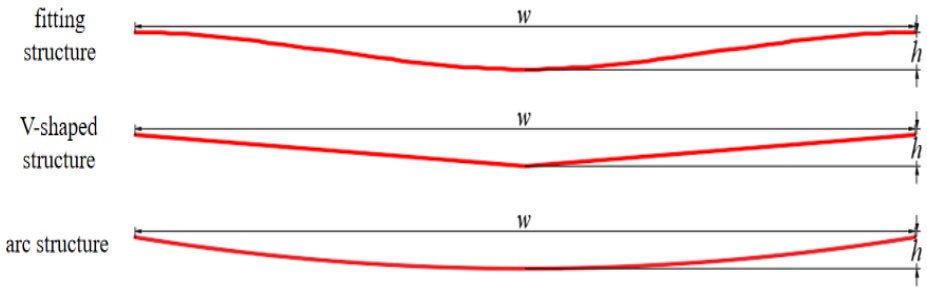

Fig. 1 2D schematic diagram of different structures

of pipelines can effectively reduce the magnitude of the pressure drop in the turbulent region (Bixler & Bhushan, 2013). They also observed that the magnitude of the pressure drop increases gradually with increasing Reynolds number.

Nonsmooth surface drag reduction technology can be applied in aerospace, ship design and other fields for reasons such as no external energy injection and significant environmental performance (Asadzadeh et al., 2019; Gu et al., 2022b). However, the current nonsmooth structures are mostly groove structures, and there is a lack of research on new structures. Therefore, to investigate the influence of new nonsmooth structures on drag reduction characteristics, inspired by the beluga whale skin ridge structure, a bionic fitting structure is designed with a flat plate as a carrier, and the drag reduction characteristics and mechanisms of the fitting structure, V-shaped structure, arc structure and parameters of the fitting structure are compared. This study provides a theoretical basis and design ideas for the design of overcurrent components in ship engineering and small navigational vehicles.

2. MODELING AND NUMERICAL SIMULATION METHODS

2.1 Biomimetic Nonsmooth Modeling

To better pursue prey, whales have evolved the ability to swim extremely quickly, reaching speeds of up to 50 kilometers per hour, while moving nimbly. Faster speeds tend to generate greater drag, and it is of interest to study drag-reducing structures on whales' body surfaces. Investigations have revealed that certain areas of its skin surface are adorned with wavy and regular ridges, known as dermal ridges. Microscopic measurements of histological sections (Wainwright et al., 2019) revealed that the dermal ridges of beluga whales are distributed nearly perpendicular to the flow direction on the skin surface. The cross-sectional shape of these ridges resembles a sine wave.

The dermal ridges of beluga whales (Shoemaker & Ridgway, 1991) have adjacent peak spacings of approximately 0.41-2.35 mm and heights of 7-112 μm. Considering practical processing and application, three nonsmooth structures are proposed based on the reconstruction of their biological features. Figure 1 shows the fitting structure, the V-shaped structure, and the arc structure, whose main structural parameters are the width w and depth h. The initial structural dimensions are selected as w=18 mm and h=0.5 mm. The fitting structure is obtained by using cubic spline interpolation (with 15 control points) to curve-fit the three fixed points, resulting in a structure that closely resembles the biomimetic dermal ridges.

To study the resistance of a flat plate surface, the fluid medium in typical calculation domains is water at room temperature, and usually, the flow model of a flat plate surface in a rectangular pipe shows turbulent flow at a Reynolds number of 5×10^5. The minimum inflow velocity is set to 12 m/s. According to the Reynolds number, the length of the flow direction of the calculation domain should be greater than 50 mm to achieve turbulent flow. Considering the arrangement of the nonsmooth structure, the length of the flow direction is 120 mm, and the width of the spreading direction is 20 mm. After repeated testing, the calculation domain height is set to Z = 40 mm. The formula for calculating the thickness of the boundary layer of a flat plate is as follows (Chen et al., 2023). The boundary layer thickness is calculated to be 2.6 mm.

$$\delta = 0.37LRe^{-0.2} \tag{1}$$

Three structures are arranged on a smooth flat plate, and the arrangement area is a rectangular plane intercepted on the flat plate with a length l=90 mm and a width Y=20 mm. The arrangement position is at a distance d_1=15 mm from the inlet and at a distance d_2=15 mm from the outlet. A schematic diagram of the arrangement of the three structures is shown in Fig. 2.

2.2 Numerical Simulation and Boundary Parameterization

The numerical simulation uses the incompressible Navier–Stokes governing equations. Due to the use of wall functions, the traditional k–epsilon model cannot simulate the viscous sublayer and transition layer in the boundary layer. Due to the study of frictional resistance between the fluid and wall, the calculation accuracy of the boundary layer is relatively high. Therefore, the SST k-ω model based on the Reynolds-averaged Navier–Stokes (RANS) method is selected as the numerical calculation model for wall resistance, and the simulation is performed in Fluent software. The velocity inlet condition is set to the left of the computational domain. Considering that the sailing speed of ships and speedboats is approximately 12-

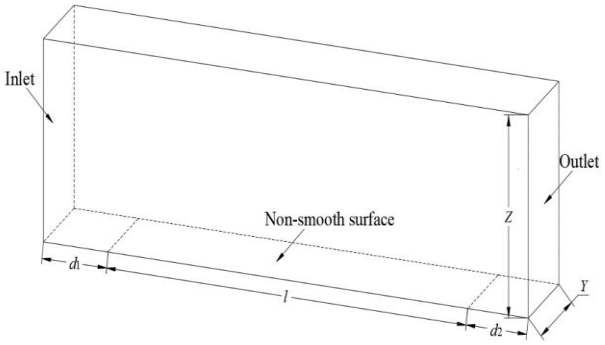

(a)Schematic diagram of the calculation domain model for the non-smooth structure.

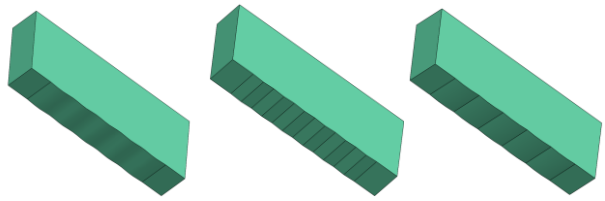

(b)Fitting structure (c)V-shaped structure (d)Arc structure

Fig. 2 Schematic diagram for the arrangement of non-smooth structures

20 m/s, the main flow velocity is selected to be 12-20 m/s. The right exit of the computational domain adopts the mass exit boundary condition, which is suitable for describing less clear exit velocity and pressure profiles, because the model can be adapted based on the flow calculation problem that is fully developed in the computational domain. The upper wall, the smooth flat surface and the subsequently used nonsmooth structural surface of the calculation domain are all set as no-slip conditions, and the left and right sidewalls are set as symmetric.

2.3 Mesh Segmentation and Reliability Verification

A structured mesh is used to divide the computational model, and due to the study of the near-wall resistance problem, the mesh quality of the near-wall surface directly affects the accuracy of the computational results. Generally, when the SST k-ω model is used to solve the problem, $y^+ < 3$ is required to satisfy the computational requirements, so the first layer mesh height Δy can be estimated by the value of y^+ to improve the accuracy of the results. Δy is estimated according to $y^+ < 3$, and Δy is calculated as follows (Li et al., 2017):

$$\Delta y = L y^+ \sqrt{80} Re^{-\frac{13}{14}} \tag{2}$$

The simulations revealed that the overall mesh

Table 1 Mesh irrelevance study

Δy(mm)	Total meshes(10^4)	Total resistance (N)	relative error(%)
0.01	55	1.854	3.79
0.007	60	1.851	3.61
0.004	80	1.802	0.85
0.001	130	1.787	—

encryption in the transverse and longitudinal directions had little effect on the calculation results, while changing the near-wall mesh partitioning method could substantially affect the calculation results; therefore, mesh irrelevance studies were carried out by setting Δy to 0.001 mm, 0.004 mm, 0.007 mm and 0.01 mm, with the overall mesh quality remaining the same. A flow rate of 20 m/s was selected, and the results of the four calculations are shown in Table 1. Comparing the resistance values obtained from each kind of mesh calculation with the resistance values obtained from the finest mesh reveals that the difference between the calculation results of the first layer mesh heights of 0.004 mm and 0.001 mm is 0.85%, while the difference between 0.007 mm and 0.01 mm is approximately 3.5%. The comprehensive consideration is to choose a Δy of 0.004 mm and a nearly wall growth rate of 1.1 as the mesh division parameters.

To calculate the friction coefficient C_f on a smooth flat plate surface, the friction coefficient can be compared using a theoretical and empirical formula. A corresponding formula is as follows (Tang et al., 2022):

$$C_f = 0.074 Re^{-\frac{1}{5}} \tag{3}$$

The results of the turbulence model calculations compared with the empirical theoretical values are shown in Table 2. The overall calculation error of the SST k-ω model does not exceed 5%, which meets the requirements of engineering calculations.

3. EFFECT OF THE NONSMOOTH STRUCTURE ON THE FLOW RESISTANCE

The total wall resistance usually consists of viscous resistance and pressure resistance.

The viscous resistance is calculated as follows (Li et al., 2017):

$$f = \int \tau \mathrm{d}A = \sum_{i=1}^{n} \tau_i \left| A_i \right| \tag{4}$$

Table 2 Comparison results between simulated and theoretical values

velocity of flow(m/s)	Reynolds number(10^6)	C_f theoretical value(10^{-3})	SST k-ω simulated value(10^{-3})	Error(%)
12	1.43	4.31	4.13	4.23
16	1.91	4.07	3.91	3.99
20	2.38	3.89	3.76	3.46

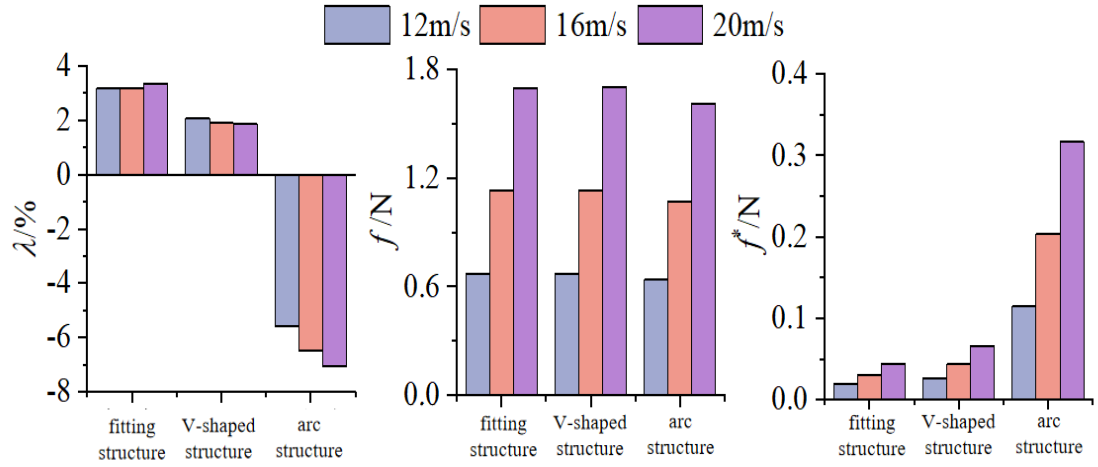

(a)Drag reduction rate (b)Viscous resistance (c)Pressure resistance

Fig. 3 Comparison of drag reduction effects among different structures

where f is the viscous resistance, N; τ_i is the discrete cell shear stress, N; and A_i is the wall discrete cell area, m^2.

The pressure resistance is derived from the hydrostatic pressure and is calculated as follows (Li et al., 2017):

$$f^* = \int \sigma \mathrm{d}A^* = \sum_{i=1}^{n} \sigma_i \left| A_i^* \right| \tag{5}$$

where f^* is the pressure resistance, N; σ_i is the discrete cell compressive stress, N; and A_i^* is the projected area of the trench surface along the main flow field, m^2.

The following formula is used to calculate the total wall resistance F:

$$F = f + f^* \tag{6}$$

The drag reduction rate λ is defined as:

$$\lambda = \frac{F_1 - F_2}{F_1} \times 100\% \tag{7}$$

where F_1 is the total resistance on the smooth flat surface and F_2 is the resistance on the biomimetic structure surface.

The drag reduction effects of the three nonsmooth structures are simulated at different main flow field velocities, and the comparative results are shown in Fig. 3. Figure 3(a) shows that the drag reduction rate of the fitting structure is greater than that of the V-shaped structure and the arc structure at flow velocities of 12 m/s, 16 m/s and 20 m/s, which yields the greatest drag reduction effect. The drag reduction rate of the fitting structure increases with increasing flow velocity, but the overall increase is not large, and the drag reduction rate is greater than 3%. The drag reduction rate of the V-shaped structure decreases with increasing flow velocity, but the decrease is small, which also indicates that the influence of flow velocity on the V-shaped structure is weak, and its drag reduction rate is maintained at approximately 2%. The drag reduction effect of the arc structure is negative, i.e., not only does it not produce a resistance reduction effect but also increases the resistance so that it becomes a resistance increasing effect. With increasing flow velocity, the resistance increase effect becomes increasingly clear, and the drag reduction effect becomes less than -5%.

The viscous resistance values f are shown in Fig. 3(b). The viscous resistance values of the three structures increase with increasing flow rate, and there is not much difference in the viscous resistance values of the fitting structure and the V-shaped structure under the same flow rate; however, the three flow rates of the arc structure are smaller than those of the fitting structure and the V-shaped structure, which also indicates that the arc structure is slightly better than the other two structures in terms of reducing the viscous resistance. The pressure resistance of the three different structures is shown in Fig. 3(c). The pressure resistance of all three structures increases with increasing flow velocity. The pressure resistance of the fitting structure is smaller than that of the arc and V-shaped structures for all three flow velocities. The change in pressure resistance of the fitting structure is the smallest, and that of the arc structure is the largest as the flow velocity increases. When the pressure resistance of the arc structure is too large, the overall drag reduction effect is worse than that of the fitting structure and the V-shaped structure, and increased resistance may even occur. The overall drag reduction effect of the three structures is best achieved by the fitting structure, with the minimum increase in pressure resistance, and the influence of the structural parameters on the drag reduction effect is further analyzed by taking considering fitting structure as the research object.

The drag reduction effect of the fitting structure is better than that of the V-shaped structure and the arc structure at a flow velocity of 20 m/s. To further account for this, the flow field of the fitting structure is analyzed. Figure 4 shows the comparison of the compressive stresses of different structures at a flow velocity of 20 m/s

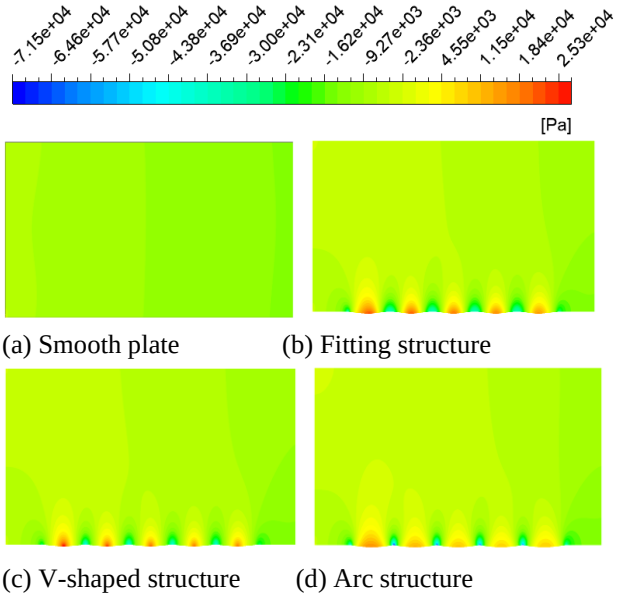

(a) Smooth plate (b) Fitting structure

(c) V-shaped structure (d) Arc structure

Fig. 4 Compressive stress cloud for different structures

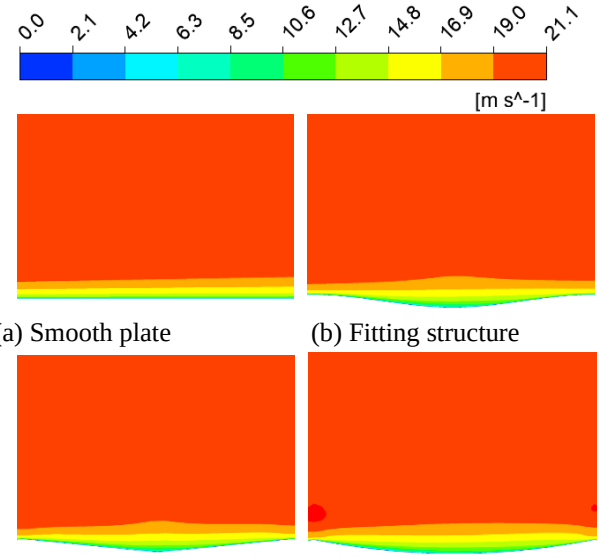

(a) Smooth plate (b) Fitting structure

(c) V-shaped structure (d) Arc structure

Fig. 5 Velocity cloud for different structures

(spreading to the center cross-section, the same as below). Compared with those of the smooth flat plate, the three nonsmooth structures are all high-pressure stress regions (dark red region) at the depression and low-pressure stress regions (dark green region) at the bulge; this tendency presents a type of periodic change. In terms of the changes in the compressive stress gradient, the arc structure exhibits the largest change, in which the low-pressure region at its bulge has changed as reflected by the dark blue color, while there is no clear difference in the change in the compressive stress gradient between the V-shaped structure and the fitting structure. A significant change in the compressive stress gradient leads to an increase in the pressure resistance of the arc structure.

Figure 5 shows the velocity clouds of different structures (the first nonsmooth structure cell is intercepted along the flow direction), which shows that due to the viscous interaction between the fluid and the wall, a velocity gradient difference is generated near the wall surface. Comparing the smooth structure and three nonsmooth structures, due to the presence of the nonsmooth structure, the boundary layer of the fluid on the nonsmooth surface becomes thicker, which slows the velocity of the fluid on the surface of the object, thus reducing the viscous drag on its surface.

Figure 6 shows the comparison of shear stresses among different structures (the bottom surface of the basin). The low shear stress area (dark blue area) of the nonsmooth structures is significantly larger than that of the smooth structure, which explains the lower viscous resistance. The shear stress at the depression is lower, and the shear stress at the bulge is higher for all three structures. The area of the low shear stress region for the fitting structure and V-shaped structure is less than that of the arc structure. However, the area of the high shear stress region for the arc structure is simultaneously larger than that of the others, which also leads to a smaller difference in the viscous drag value. In terms of the distribution of low shear stress areas, the low shear stress areas of the fitting and V-shaped structures are mainly distributed at the bottom of the structure, while the low shear stress areas of the arc structure are distributed in the structure near the incoming flow direction, and the shear stresses at the bulge are significantly greater than those of the fitting and V-shaped structures.

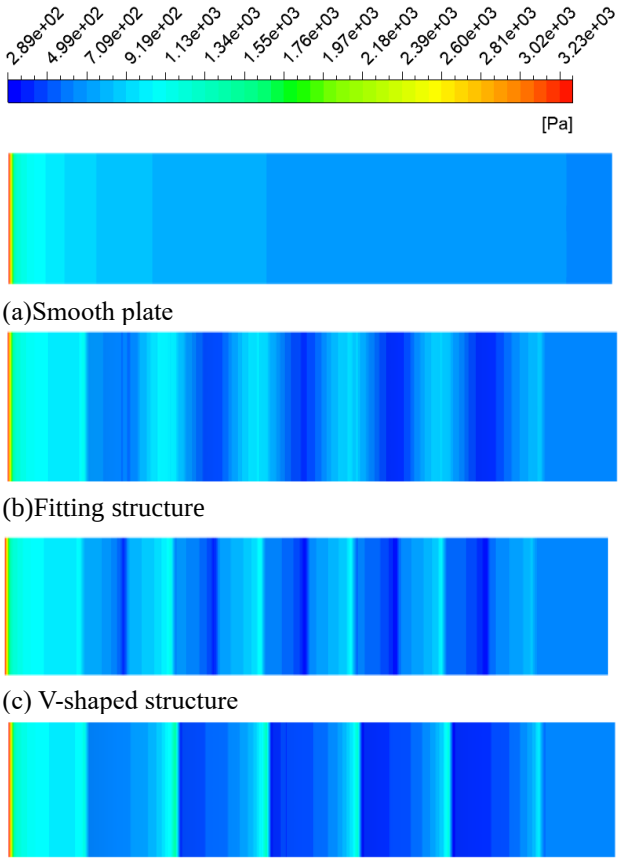

(a)Smooth plate

(b)Fitting structure

(c) V-shaped structure

(d) Arc structure

Fig. 6 Shear stress cloud for different structures

Table 3 Calculation scheme of the fitting structure for different widths and depths

*h**w*	12.86 mm	15 mm	18 mm	22.5 mm	30 mm
0.3 mm	*w*12.86*h*0.3	*w*15*h*0.3	*w*18*h*0.3	*w*22.5*h*0.3	*w*30*h*0.3
0.4 mm	*w*12.86*h*0.4	*w*15*h*0.4	*w*18*h*0.4	*w*22.5*h*0.4	*w*30*h*0.4
0.5 mm	*w*12.86*h*0.5	*w*15*h*0.5	*w*18*h*0.5	*w*22.5*h*0.5	*w*30*h*0.5
0.6 mm	*w*12.86*h*0.6	*w*15*h*0.6	*w*18*h*0.6	*w*22.5*h*0.6	*w*30*h*0.6
0.7 mm	*w*12.86*h*0.7	*w*15*h*0.7	*w*18*h*0.7	*w*22.5*h*0.7	*w*30*h*0.7

4. INFLUENCE OF WIDTH AND DEPTH ON THE DRAG REDUCTION EFFECT

To ensure comparability of the drag reduction effects across different widths and depths, the arrangement area of the fitting structure is kept constant, and the widths *w* are chosen to be 12.86 mm, 15 mm, 18 mm, 22.5 mm and 30 mm, i.e., the numbers of fitting structures n are 7, 6, 5, 4, and 3. When the depth of the nonsmooth structure is less than the thickness of the boundary layer, the desired drag reduction effect can be achieved; considering the depth of the surface skin of the beluga whale, the depths h are chosen to be 0.4 mm, 0.5 mm, 0.6 mm, 0.7 mm and 0.8 mm. A uniform numbering is developed, e.g., the significance of *w*12.86*h*0.4 is the fitting structures with width *w*=12.86 mm and depth *h*=0.4 mm. A total of 25 kinds of fitting structure programs were used for the calculations, and the specific program is shown in Table 3.

4.1 Influence of Width on Drag Reduction of the Fitting Structure

Under a flow velocity of 20 m/s, the change curves of the drag reduction rate with width are shown in Fig. 7. At depths of *h*=0.3 mm and 0.4 mm, the fitting structures at these two depths exhibit drag reduction at five different widths, and the drag reduction rate changes gradually. At a depth of *h*=0.3 mm, the drag rate decreases with increasing width; at a depth of *h*=0.4 mm, it reaches a peak at width *w*=15 mm and then decreases slightly; at a depth of *h*=0.5 mm, the drag reduction effect occurs at all five widths and increases and then decreases with width, and the rate reaches its maximum value at width *w*=18 mm; at depths *h*=0.6 mm and 0.7 mm, the trend of the drag reduction rate with increasing width is essentially the same, and it maintains a rising trend; overall, *w*12.86*h*0.7 and *w*12.86*h*0.6 are negative, which means that the effect of increasing drag is produced, and all the remaining schemes have a drag reduction effect, of which *w*30*h*0.7 has the greatest drag reduction effect, with a rate of 4.18%.

The viscous resistance *f* and pressure resistance *f** with different widths are shown in Fig. 8. The viscous resistance *f* of the five depths all show a rising trend with increasing width, which is unfavorable for drag reduction. When the depth h is smaller, the viscous resistance shows a more gradual increasing trend, which indicates that for greater depths, increasing the width clearly increases the viscous resistance and weakens the effect of drag reduction. The figure shows that the pressure resistance at the five depths decreases with increasing width, and at the same width, the greater the depth is, the greater the pressure resistance, and the greater the depth is, the more

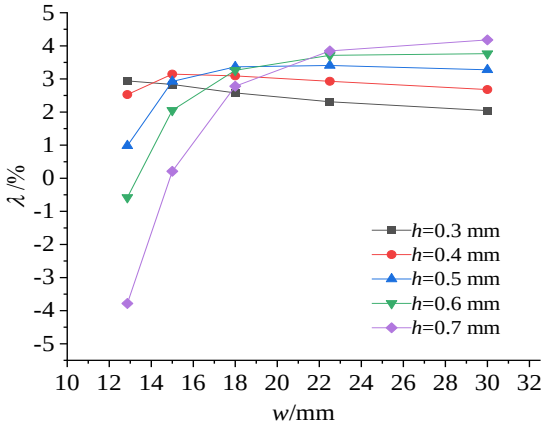

Fig. 7 Curves of drag reduction rate with width of the fitting structure

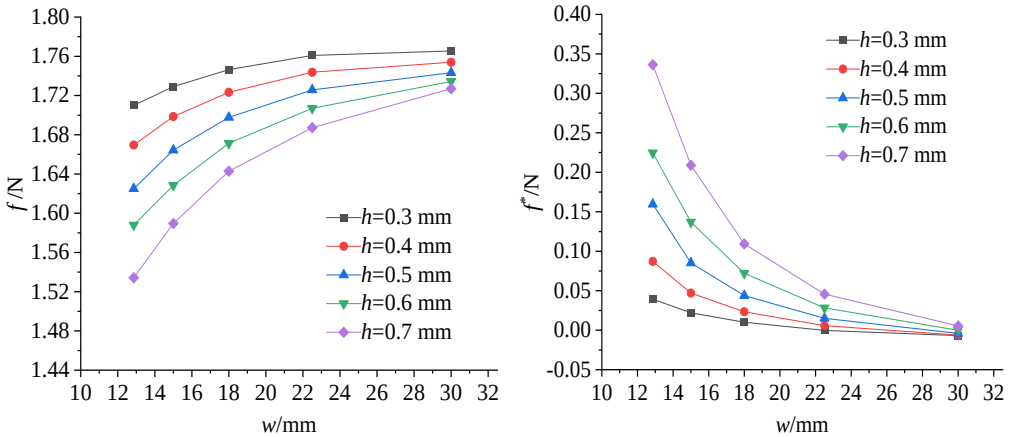

(a) Viscous resistance (b) Pressure resistance

Fig. 8 Curves of viscous resistance and pressure resistance with width of the fitting structure

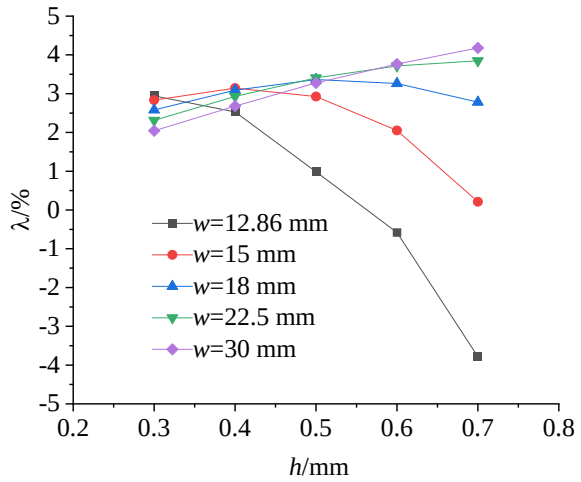

Fig. 9 Curves of drag reduction rate with depth of the fitting structure

significant the trend of the pressure resistance with increasing width, which indicates that when the depth is fixed, increasing the width of the fitting structure can effectively reduce the pressure resistance, thereby increasing its drag reduction effect, and this effect becomes more clear at greater depths. For all the fitting structures with different schemes, when the depth is fixed, the viscous resistance increases with increasing width, but the pressure resistance decreases. If the decrease in pressure resistance is greater than the increase in viscous resistance, then the drag reduction effect can be enhanced, i.e., the drag reduction rate λ increases.

4.2 Influence of Depth on Drag Reduction of the Fitting Structure

Under a flow velocity of 20 m/s, the change curves of the drag reduction rate with depth are shown in Fig. 9. When the width is w=12.86 mm, the drag reduction rate shows a significant decreasing trend with increasing depth, and when the depth is h≤0.5 mm, all the structures experience a drag reduction effect, reaching a maximum value of 2.94% when h=0.3 mm. When the width is w=15 mm or 18 mm, the two widths have drag reduction effects at five different depths, and the drag reduction rate shows the same tendency to increase and then decrease. For width w=15 mm, the drag reduction rate reaches a maximum value of 3.14% at h=0.4 mm. For width w=18 mm, the drag reduction rate increases with depth as the depth h=0.3-0.5 mm varies, and the maximum value is 3.36%; then, it starts to decrease slowly. For widths w=22.5 mm and 30 mm, the trend of drag reduction with depth is similar, and it increases with depth for both widths, reaching a maximum at a depth h=0.7 mm and width w=30 mm.

The viscous resistance f and pressure resistance f^* with different depths are shown in Fig. 10. The viscous resistances of the fitting structures with different widths all exhibits the same tendency, i.e., the larger the depth is, the smaller the viscous resistance, which increases the drag reduction effect, and the smaller the width w is, the more significant the effect of the depth on the viscous resistance. In terms of pressure resistance, the figure shows that the pressure resistance increases with increasing depth, and similarly, the smaller the width w *is*, the more significant the effect of depth is. When the width w = 30, the effect of different depths on the pressure resistance is very weak and almost unchanged, and when the depth h is less than or equal to 0.6 mm, the pressure resistance is negative, indicating that the pressure resistance is converted into a dynamic force, which pushes on the nonsmooth surface and thus reduces its surface resistance.

5. SURFACE FLOW FIELD OF THE FITTING STRUCTURE

The combinations with large variations in drag reduction rates are convenient for observing surface flow field changes; therefore, fitting structures with widths w of 12.86 mm, 18 mm, and 30 mm and depths h of 0.7 mm were selected to analyze the effect of width on the flow field. Fitting structures with depths h of 0.3 mm, 0.5 mm, and 0.7 mm and widths w of 12.86 mm were selected to analyze the effect of depth on the flow field. The change in the flow field under different parameters is analyzed to summarize the drag reduction mechanism of the fitting structure.

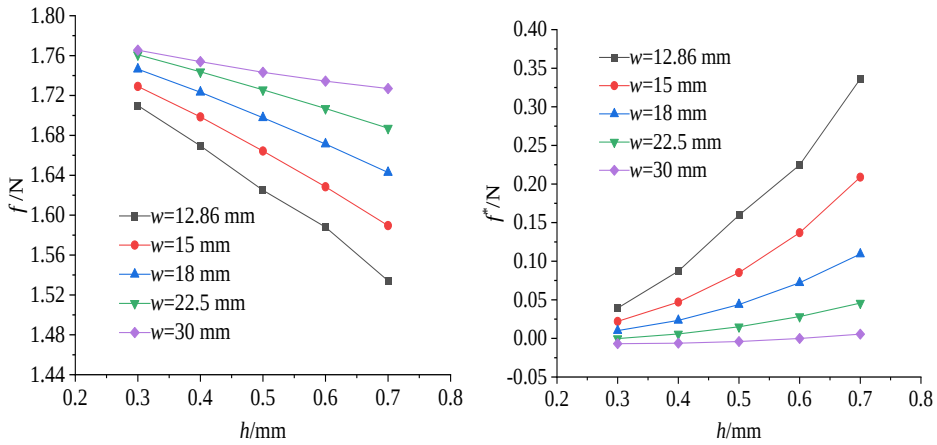

(a) Viscous resistance (b) Pressure resistance

Fig. 10 Curves of viscous resistance and pressure resistance with depth of the fitting structure

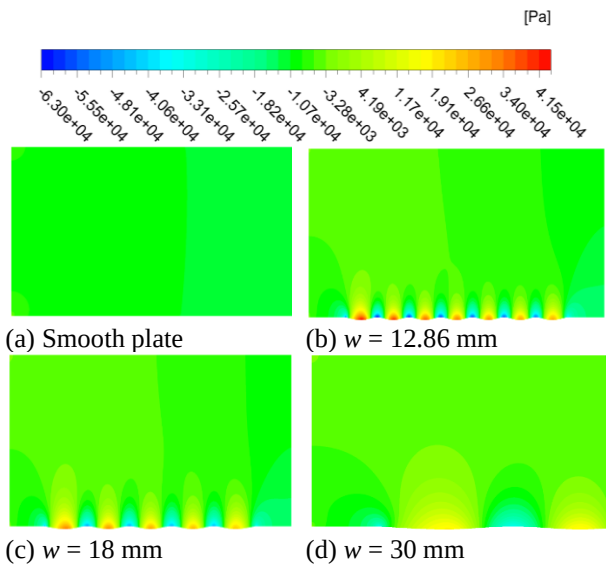

(a) Smooth plate (b) w = 12.86 mm

(c) w = 18 mm (d) w = 30 mm

Fig. 11 Contour plots of compressive stress for fitting structure with different widths

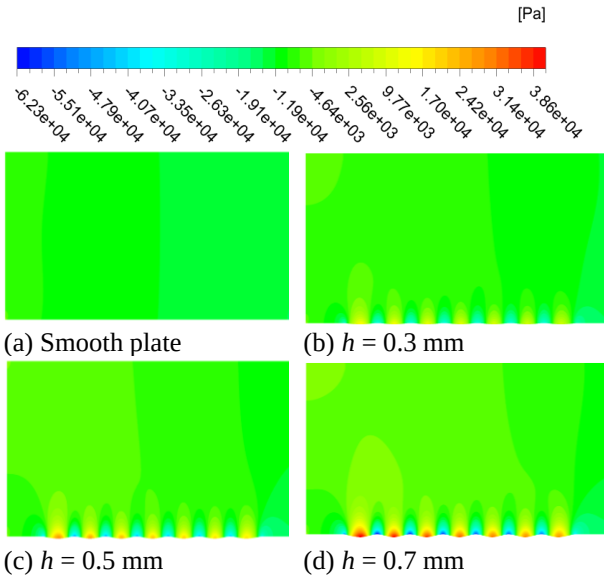

(a) Smooth plate (b) h = 0.3 mm

(c) h = 0.5 mm (d) h = 0.7 mm

Fig. 12 Contour plots of compressive stress for fitting structure with different depths

5.1 Compressive Stress Analysis

The pressure resistance is closely linked to the compressive stress, and the compressive stress on the surface affects the change in pressure resistance. Contour plots of the compressive stress for fitting structures with different widths are shown in Fig. 11. The data show that the pressure distribution of the fitting structure is very inhomogeneous compared with that of the smooth flat plate, and there is a significant pressure difference in the local region of the fitting structure, but it shows a better regularity, i.e., the depression is always a high-pressure stress region, and the bulge shows a low-pressure stress region, which exhibits a cyclic transformation. Comparing the contour plots of compressive stress with different widths, it can be seen that the fitting structures with larger widths have smaller changes in pressure stress gradients, while the fitting structures with smaller widths have larger changes in pressure stress gradients. Due to the relationship between pressure stress gradients and pressure resistance, the fitting structures with larger widths have smoother surfaces and smaller pressure resistance. Therefore, as the width increases, the variation in the compressive stress gradient gradually tends to flatten.

Figure 12 shows contour plots of the compressive stress for fitting structures at different depths, and the change in the compressive stress gradually increases with increasing depth for the same width. The pressure resistance of the fitting structure with a greater depth is significantly greater than that with a smaller depth, so a large gradient of the compressive stress is associated with a large pressure resistance.

5.2 Velocity Field Analysis

Figure 13 shows the velocity variation cloud for fitting structures with different widths. The fitting structures with different widths change the distribution of the boundary layer on their near-wall surfaces, and the thickness of the boundary layer decreases as the width increases, which leads to an increase in the velocity gradient on the near-wall surfaces and an intensification of the interaction between the fluid and the wall surfaces, which ultimately results in an increase in the viscous drag. The width w=12.86 mm has the lowest value, and the corresponding velocity cloud boundary layer thickness is also larger. The width w=30 mm has the highest value of viscous drag, and the corresponding velocity boundary layer thickness is the smallest.

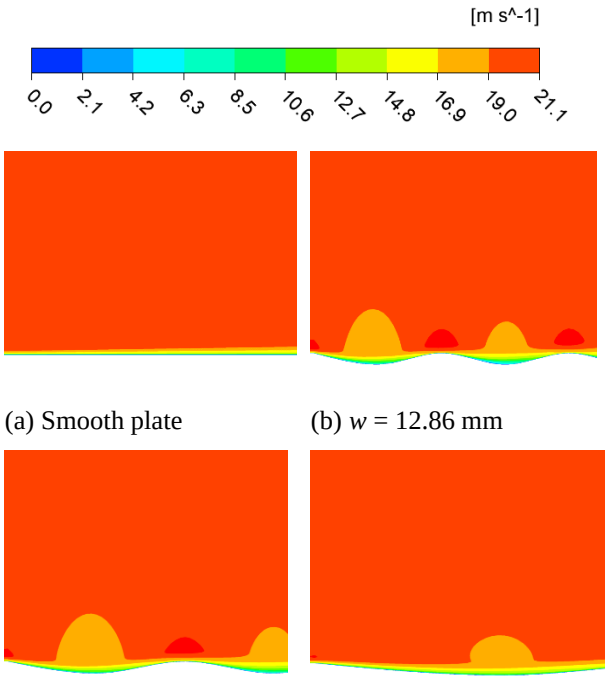

(a) Smooth plate (b) w = 12.86 mm

(c) w = 18 mm (d) w = 30 mm

Fig. 13 Velocity variation cloud for fitting structures with different widths

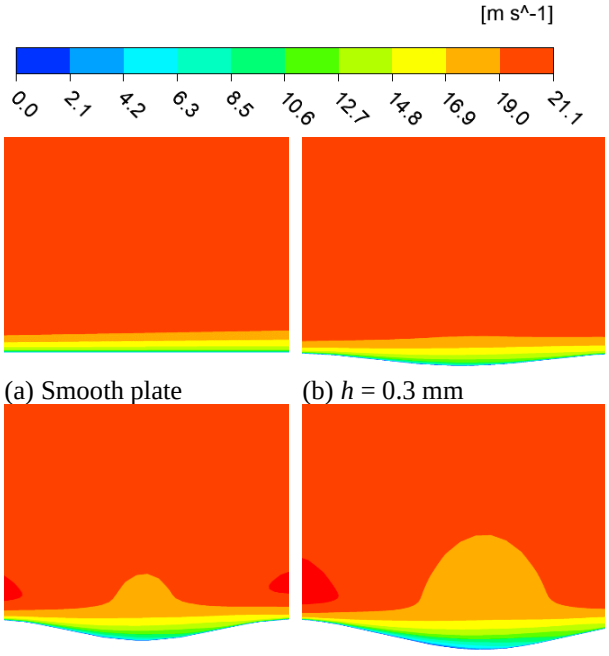

(a) Smooth plate (b) h = 0.3 mm

(c) h = 0.5 mm (d) h = 0.7 mm

Fig. 14 Velocity variation cloud for the fitting structures with different depths

Figure 14 shows the velocity variation cloud for the fitting structures with different depths. The thickness of the boundary layer of the fitting structures at different depths changes, it increases with depth, and the low-velocity fluid increases, which converts the friction between the high-velocity fluid and the surface of the object into friction between the high-velocity and the low-velocity fluid and serves as a kind of lubricant-like effect that reduces the viscous resistance of the object surface. The viscous drag is the largest at a depth of 0.3 mm, which corresponds to the minimum thickness of the boundary layer of the velocity cloud, and the viscous drag is the smallest at a depth of 0.7 mm, which corresponds to the maximum thickness of the boundary layer of the velocity cloud. The nonsmooth structural unit increases the thickness of the bottom boundary layer and reduces the velocity at its surface, thus providing a drag reduction effect.

5.3 Shear Stress Analysis

The shear stress variation cloud for fitting structures with different widths is shown in Fig. 15. The fitting structure with different widths has a larger area of the overall low shear stress region (the dark blue part) compared with the smooth structure, which to some extent explains the reduction in the viscous resistance of the fitting structure. Comparing the surface shear stresses of the fitting structures with different widths reveals that the shear stresses exhibit periodic changes, with smaller shear stresses at the depressions and larger shear stresses at the bulge of the fitting structures. The gradient of the shear stress is more pronounced for smaller widths, while it tends to flatten for larger widths. Overall, the low shear stress region decreases with increasing width, so a fitting

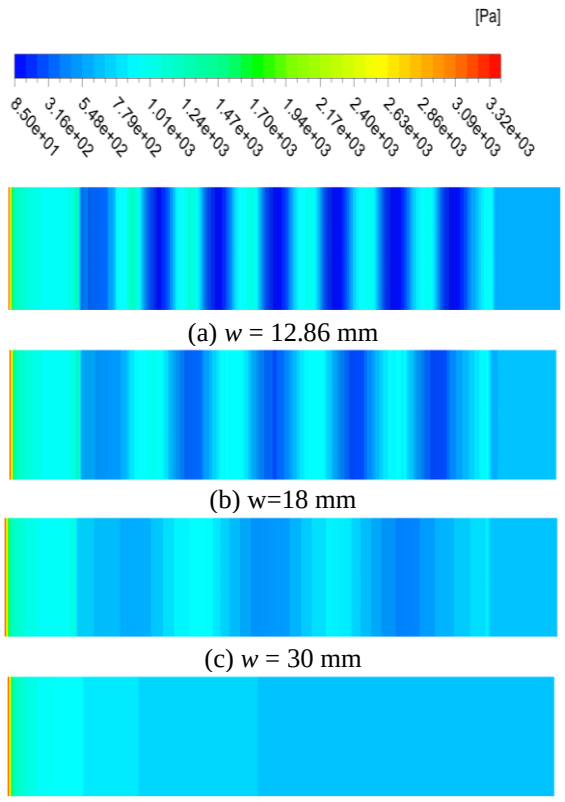

(a) w = 12.86 mm

(b) w=18 mm

(c) w = 30 mm

(d) Smooth plate

Fig. 15 Shear stress variation cloud for fitting structures with different widths

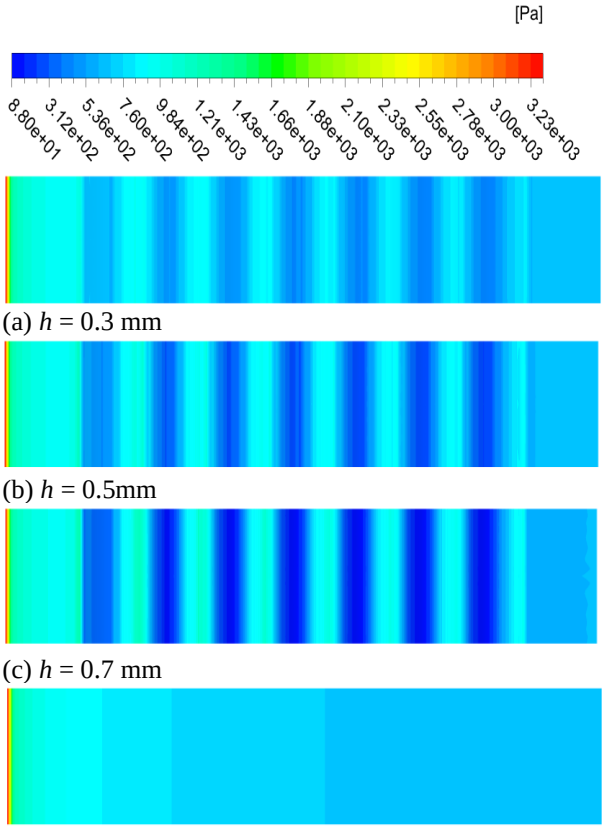

(a) h = 0.3 mm

(b) h = 0.5mm

(c) h = 0.7 mm

(d) Smooth plate

Fig. 16 Shear stress variation cloud for fitting structures with different depths

structure with a smaller width has more advantages in reducing the shear stress at the same depth.

The shear stress variation cloud for fitting structures with different depths is shown in Fig. 16. From the surface of the fitting structures, the area of the low shear stress region (dark blue part) is larger than that of the smooth structure, which is the main reason why the viscous resistance of the fitting structures is lower than that of the smooth structure. Comparing the shear stresses at different depths reveals that the shear stress gradient of the fitting structures at smaller depths changes gradually, while it changes more dramatically at larger depths, and in addition, their surface shear stresses gradually decrease with increasing depth. Overall, the low shear stress region of the fitting structure increases as the depth increases, while the shear stress simultaneously and gradually decreases. In terms of reducing the shear stress, the fitting structure with a greater depth is superior to that with a smaller depth at the same width.

6. SUMMARY

Based on the ridge-like features of the beluga skin, the skin was reconstructed and modeled as a biomimetic fitting structure. A comparative analysis of the drag reduction effects of the fitting structure, the V-shaped structure, and the arc structure revealed that the fitting structure produced the best drag reduction effect at the same flow rate. Moreover, the V-shaped structure possessed a drag reduction effect, while the arc structure produced a drag increase effect. Although the fitting structure's viscous resistance reduction is not optimal, its pressure resistance is the smallest. Overall, its resistance is the smallest, and the fitting structure has the best drag reduction effect.

At the same depth, the viscous drag of the fitting structure gradually decreases with increasing width, and the pressure drag gradually increases; at the same width, the viscous drag of the fitting structure gradually decreases with increasing depth, and the pressure drag gradually increases. The fitting structure with a width of 30 mm and a depth of 0.7 mm produces the best drag reduction effect, with a drag reduction rate of 4.18%.

The surface of the fitting structure has a larger low shear stress region than the smooth surface, and its pressure stress gradient is too large, resulting in a change in its pressure resistance. The fitting structure increases the thickness of the bottom boundary layer, reduces the velocity of its surface, and decreases the internal fluid velocity, which converts the friction between the high-speed fluid and the surface of the object into friction between the high-speed fluid and the low-speed fluid, which plays a role similar to that of the lubricant, and reduces the viscous resistance of the object, thus providing a drag reduction effect.

ACKNOWLEDGEMENTS

This work was supported by Zhejiang Provincial Natural Science Foundation of China (NO. LY22E050015), Fundamental Research Funds for the Provincial Universities of Zhejiang (NO. 2023YW88), Zhejiang Province General Research Project Specialized for Professional Degree Graduate Students (NO. Y202353665), and Zhejiang University Student Science and Technology Innovation Activity Plan (NO. 2024R409050).

CONFLICT OF INTEREST

The authors declare that they have no known competing financial interests or personal relationships that could have appeared to influence the work reported in this paper.

AUTHORS CONTRIBUTION

Chaoxiang Hu: Writing original draft; **Yunqing Gu:** writing review; **Junjun Zhang:** Formal analysis; **Qianfeng Qiu:** Validation; **Hongxin Ding:** Formal analysis; **Denghao Wu:** Conceptualization; **Jiegang Mou:** Project administration.

REFERENCES

Asadzadeh, H., Moosavi, A., & Etemadi, A. (2019). Numerical simulation of drag reduction in microgrooved substrates using lattice-boltzmann method. *Journal of Fluids Engineering, 141*(7), 1-47. https://doi.org/10.1115/1.4042888.

Bixler, G. D., & Bhushan, B. (2013). Shark skin inspired low-drag microstructured surfaces in closed channel flow. *Journal of Colloid and Interface Science, 393*, 384-396. https://doi.org/10.1016/j.jcis.2012.10.061.

Chae, S., Lee, S., Kim, J., & Lee, J. H. (2019). Adaptive-passive control of flow over a sphere for drag reduction. *Physics of Fluids, 31*(1), 015107. https://doi.org/10.1063/1.5063908.

Chen, S. T., Yang, L. C., Zhao, W. W., & Wan, D. C. (2023). Wall-modeled large eddy simulation for the flows around an axisymmetric body of revolution. *Journal of Hydrodynamics, 35*(2), 199-209. https://doi.org/10.1007/s42241-023-0026-y.

Deng, F. Q., Cao, C., Xu, L. H., & Chi, Y. (2022). Interfacial bond characteristics of polypropylene fiber in steel/polypropylene blended fiber reinforced cementitious composite. *Construction and Building Materials, 341*, 127897. https://doi.org/10.1016/j.conbuildmat.2022.127897.

Desai, S., Prakash K, V., Kulkarni, V., & Gadgil, H. (2020). Universal scaling parameter for a counter jet drag reduction technique in supersonic flows. *Physics of Fluids, 32*(3), 036105. https://doi.org/10.1063/1.5140029.

Deshpande, R., Kidanemariam, A. G., & Marusic, I. (2024). Pressure drag reduction via imposition of spanwise wall oscillations on a rough wall. *Journal of Fluid Mechanics, 979*, A21.

https://doi.org/10.1017/jfm.2023.1062.

Gu, Y. Q., Ma, L. B., Yan, M. H., He, C. D., Zhang, J. J., Mou, J. G., Wu, D. H., & Ren, Y. (2022a). Strategies for improving friction behavior based on carbon nanotube additive materials. *Tribology International, 176*, 107875. https://doi.org/10.1016/j.triboint.2022.107875.

Gu, Y. Q., Zhang, J. J., Yu, S. W., Mou, C. Q., Li, Z., He, C. D., Wu, D. H., Mou, J. G., & Ren, Y. (2022b). Unsteady numerical simulation method of hydrofoil surface cavitation. *International Journal of Mechanical Sciences, 228*, 107490. https://doi.org/10.1016/j.ijmecsci.2022.107490.

Gu, Y. Q., Ma, L. B., Yu, S. W., Yan, M. H., Wu, D. H., & Mou, J. G. (2023a). Surface cavitation flow characterization of jet hydrofoils based on vortex identification method. *Physics of Fluids, 35*(1), 012112. https://doi.org/10.1063/5.0126564.

Gu, Y. Q., Yin, Z. F., Yu, S. W., He, C. D., Wang, W. T., Zhang, J. J., Wu, D. H., Mou, J. A., & Ren, Y. (2023b). Suppression of unsteady partial cavitation by a bionic jet. *International Journal of Multiphase Flow, 164*, 104466. https://doi.org/10.1016/j.ijmultiphaseflow.2023.104466.

Li, F., Zhao, G., & Liu, W. X. (2017). Research on drag reduction performance of turbulent boundary layer on bionic jet surface. *Part M: Journal of Engineering for the Maritime Environment, 231*(1), 258-270. https://doi.org/10.1177/1475090216642463.

Liu, G. J., Yuan, Z. C., Qiu, Z. Z., Feng, S. W., Xie, Y. C., Leng, D. X., & Tian, X. J. (2020). A brief review of bio-inspired surface technology and application toward underwater drag reduction. *Ocean Engineering, 199*, 106962. https://doi.org/10.1016/j.oceaneng.2020.106962.

Liu, Z. M., Chen, R., Tang, Z. Q., Tian, Q., Fang, Y. C., Li, P. J., Li, L., & Pang, Y. (2023). Drag reduction performance of triangular (v-groove) riblets with different adjacent height ratios. *Journal of Applied Fluid Mechanics, 16*(4), 671-684. https://doi.org/10.47176/jafm.16.04.1532.

Ma, J. W., Zhang, H., Ye, T., Wang, S. H. Z., Yang, Z. B., & Jia, Z. Y. (2024). New method of continuous-wave laser ablation for processing microgroove with variable cross-section. *Optics & Laser Technology, 170*, 110292. https://doi.org/10.1016/j.optlastec.2023.110292.

Mele, B. (2022). Riblet drag reduction modeling and simulation. *Fluids, 7*(7), 249. https://doi.org/10.3390/fluids7070249.

Meng, F., Liu, B., Zeng, Y., & Wu, W. (2016). Geometric characterization of fast shark shield scale structures. *Journal of Plasticity Engineering, 23*(02), 143-147. https://doi.org/10.3969/j.issn.1007-2012.2016.02.025.

Shoemaker, P. A., & Ridgway, S. H. (1991). Cutaneous ridges in odontocetes. *Marine Mammal Science, 7*, 66-74. https://doi.org/10.1111/J.1748-7692.1991.TB00551.X.

Tang, J., Liu, Y. Y., & Yan, Y. T. (2022). Drag reduction characteristics of bionic non-smooth surfaces for underwater vehicles. *Journal of Military Engineering, 43*(05), 1135-1143. https://doi.org/10.12382/bgxb.2021.0204.

Wainwright, D. K., Fish, F. E., Ingersoll, S., Williams, T. M., St Leger, J., Smits, A. J., & Lauder, G. V. (2019). How smooth is a dolphin? The ridged skin of odontocetes. *Biology Letters, 15*(7), 103. https://doi.org/10.1098/rsbl.2019.0103.

Wu, T., Chen, W., Zhao, A. G., He, P., & Chen, H. (2020). A comprehensive investigation on micro-structured surfaces for underwater drag reduction. *Ocean Engineering, 218,* 107902. https://doi.org/10.1016/j.oceaneng.2020.107902.

Xie, L., Jiang, L., Meng, F., Li, Q., Wen, J., & Hu, H. (2023). Development and performance of a gelatin-based bio-polysaccharide drag reduction coating. *Physics of Fluids, 35*(5), 053112. https://doi.org/10.1063/5.0149281.

Yang, Q., Zhang, Z. P., Qi, Y. H., & Zhang, H. Y. (2020). Influence of phenylmethylsilicone oil on anti-fouling and drag-reduction performance of silicone composite coatings. *Coatings, 10*(12), 1239. https://doi.org/10.3390/coatings10121239.

Yu, Q. (2021). Rewiew of drag reduction on ribs. *International Core Journal of Engineering, 7*(5), 34-37. https://doi.org/10.6919/ICJE.202105_7(5).0010.